frontiers in Astronomy and Space Sciences

ORIGINAL RESEARCH
published: 04 January 2022
doi: 10.3389/fspas.2021.786856

Blobs in a Solar EUV Jet

Jie Chen[1], Robertus Erdélyi[2], Jiajia Liu[3], Yuanyong Deng[1,4], Fionnlagh Mackenzie Dover[2], Qingmin Zhang[5], Mei Zhang[1,4], Leping Li[1] and Jiangtao Su[1,4]*

[1]Key Laboratory of Solar Activity, National Astronomical Observatories, Chinese Academy of Science, Beijing, China, [2]Solar Physics and Space Plsma Research Centre (SP2RC), School of Mathematics and Statistics, University of Sheffield, Sheffield, United Kingdom, [3]Astrophysics Research Centre, School of Mathematics and Physics, Queen's University Belfast, Belfast, United Kingdom, [4]School of Astronomy and Space Sciences, University of Chinese Academy of Sciences, Beijing, China, [5]Key Laboratory for Dark Matter and Space Science, Purple Mountain Observatory, CAS, Nanjing, China

An Extreme Ultraviolet (EUV) jet that occurred around 22:30 on July 2, 2012 was observed by the Atmospheric Imaging Assembly (AIA) on-board the Solar Dynamics Observatory (SDO). There were two phases of the jet. In Phase 1, two blobs were observed. In Phase 2, the intensity of the jet was almost coherent initially. One minute later, three blobs were formed at the same time in the jet, and the width of the jet changed after the formation of these blobs. The formation and evolution processes of the blobs in these two phases are analyzed in this paper. The physical parameters of the blobs are determined. The measured width of the blobs is 0.8 – 2.3 Mm, and the apparent velocities of the blobs are from 59 km s^{-1} to 185 km s^{-1}. The formation mechanism of the blobs is likely to be tear-mode instability.

Keywords: instabilities, magnetic reconnection, sun: activity, sun: corona, sun: jet

OPEN ACCESS

Edited by:
Dipankar Banerjee,
Indian Institute of Astrophysics, India

Reviewed by:
Vaibhav Pant,
Aryabhatta Research Institute of Observational Sciences, India
Xin Cheng,
Nanjing University, China

****Correspondence:***
Jie Chen
chenjie@bao.ac.cn

Specialty section:
This article was submitted to Stellar and Solar Physics, a section of the journal Frontiers in Astronomy and Space Sciences

Received: *30 September 2021*
Accepted: *01 December 2021*
Published: *04 January 2022*

Citation:
Chen J, Erdélyi R, Liu J, Deng Y, Dover FM, Zhang Q, Zhang M, Li L and Su J (2022) Blobs in a Solar EUV Jet. Front. Astron. Space Sci. 8:786856. doi: 10.3389/fspas.2021.786856

1 INTRODUCTION

Solar jets are thought to play an important role in solar wind acceleration and coronal heating (e.g., Tian et al., 2014; Cirtain et al., 2007). In the solar atmosphere, jet-like events are very common with a wide range of physical parameters observed at a broad range of wavelengths. Both hot and cool plasma exhibit jet-like ejections, such as chromospheric spicules (e.g., Beckers, 1968; Sterling, 2000; Zaqarashvili and Erdélyi, 2009; Tsiropoula et al., 2012); chromospheric Hα surges (e.g., Schmieder et al., 1995; Canfield et al., 1996; Uddin et al., 2012); choromospheric CaII K jets (e.g., Morita et al., 2010; Morton 2012); coronal Extreme Ultraviolet (EUV) jets (e.g., Li et al., 2012; Morton et al., 2012; Liu et al., 2016a; Hong et al., 2016; Hong et al., 2017; Zhang and Zhang. 2017; Liu et al., 2018); macrospicules (e.g., Scullion et al., 2009; Scullion et al., 2011; Kayshap et al., 2013; Kiss et al., 2017), coronal X-ray jets (e.g., Moore et al., 2010; Huang et al., 2012; Liu et al., 2016b). It is generally considered that coronal jets are heated by magnetic reconnection (e.g., Yokoyama and Shibata, 1995). Jet activities are commonly associated with flux emergence and cancellation (e.g., Liu & Kurokawa 2004). Besides the ordinary collimated motions, jets often exhibit helical structure and untwisting motions (Shen et al., 2011; Shen et al., 2012). In addition to helical and untwisting motions, jet displays the swaying motions (transverse oscillations) (Sarkar et al., 2016). Jets may also be formed by shock waves (e.g., De Pontieu et al., 2004). Detailed descriptions of coronal jets can be found in recent reviews (Innes et al., 2016; Raouafi et al., 2016; Shen, 2021).

Plasmoids (or magnetic islands or blob-like structures) are ubiquitous in the solar atmosphere. In magnetic reconnection theory, a current sheet in an antiparallel magnetic field is unstable which may form plasmoids due to the tearing-mode instability (Kliem et al., 2000; Lin et al., 2005; Ni et al., 2015). The ejection of plasmoid may induce the intermittent enhancement of the reconnection rate.

Lin et al. (2005) reported direct observations of the magnetic reconnection site in an energetic partial-halo coronal mass ejection (CME). Recently, Liu et al. (2016b) presented a detailed analysis of recurrent homologous jets. Recurrent jets are a result of recurrent magnetic reconnection (the different reconnection events). It is only possible when the time interval of recurrent jets is comparable with that of the outflow jets ejected out of the unsolved current sheet (e.g., Cheng et al., 2018). A recent and detailed statistical analysis on the blobs in EUV formed in the post-CME current sheet is given in Patel et al. (2020). During magnetic reconnection in solar flares, many observations exhibit that plasmoids are formed in current sheet (Asai et al., 2001; Liu et al., 2009; Takasao et al., 2012). The blobs during a breakout reconnection were also very recently observed by (Kumar et al., 2019).

Blob-like structures can form not only in current sheet, but also in solar jets. Singh et al. (2012) observed bright plasma ejecta in chromospheric anemone jets with the Solar Optical Telescope (SOT) on board Hinode using Ca II H filtergram. The typical lifetime of the plasma ejecta is about 20–60 s with a size about 0.3–1.5 Mm for chromospheric jets, and with a speed of ~35 km s^{-1} of downward moving blobs. Yang et al. (2013) constructed a 2.5-dimensional numerical MHD model to simulate chromospheric anemone jets. Due to the tearing mode instability, plasmoids are generated during the reconnection process that are consistent with the observed moving bright blobs in anemone jets. Zhang & Ji (2014) reported the discovery of blobs in recurrent and homologous EUV jets. In their study, there is evidence for only one blob in one jet. They found the median temperature of the blobs ~2.3 MK with diameter of ~3 Mm and lifetimes 24–60 s. Zhang et al. (2016) observed the blobs of EUV jets with size of ~1.7 Mm and an apparent velocity of ~238 km s^{-1}. They also found that the blobs have a temperature of 1.8–3.1 MK. The estimated the number density of the blobs was (1.7–2.8) × 10^9 cm^{-3}. In one particular jet, multiple blobs are observed. However, the blobs are observed by Extreme Ultraviolet Imager (EUVI) on-board the Solar Terrestrial Relations Observatory (STEREO), with spatial resolution of 1.6″/$pixel^{-1}$. Therefore, the blobs can not be seen clearly. Through performing 2D resistive MHD simulations of coronal jets, Ni et al. (2017) showed that the plasmoid instability and Kelvin-Helmholtz instability along the jet are possible formation mechanisms of blobs observed in EUV wavelengths.

Chen et al. (2017) observed a complex jet with two intrinsic phases to the west of NOAA AR 11 513 on July 2, 2012 with high spatial resolution using data obtained by Atmospheric Imaging Assembly (AIA) (Lemen et al., 2012) on-board the Solar Dynamics Observatory (SDO) and analyzed the driving mechanism of the jet. In this paper, we report the observation of multiple blobs and analyze the evolution of the detected blobs in the complex jet which were studied by Chen et al. (2017). We also investigate the physical properties of these jets and present possible mechanisms responsible for the evolution of the jet. In **section 2**, we outline the observations, the method is described in **Section 3**, and in **Section 4** we detail the results. In the last section, we provide critical discussions and draw summarizing conclusions.

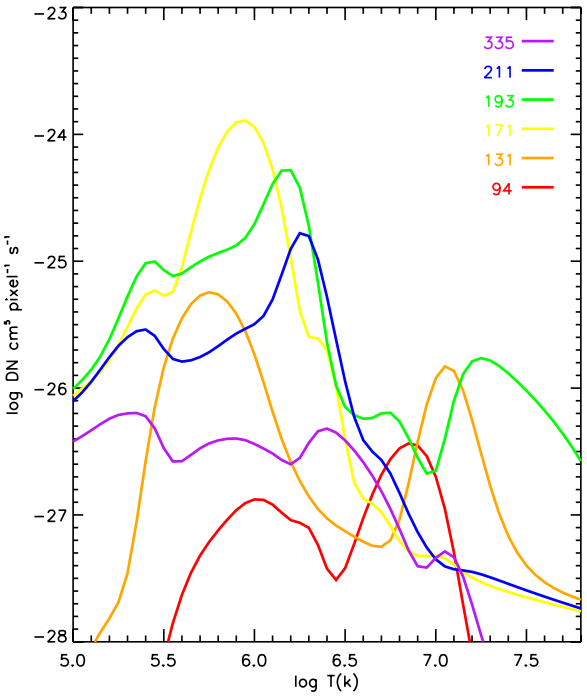

FIGURE 1 | AIA temperature response curves from SSW routine (aia_get_response.pro) showing the temperature sensitivity of the different filters with 94 Å (red), 131 Å (orange), 171 Å (yellow), 193 Å (green), 211 Å (blue), 335 Å (purple).

2 INSTRUMENTS AND DATA REDUCTION

In this study, we use the observation by the AIA telescope on-board SDO which has a spatial resolution of 0.″6 $pixel^{-1}$. The AIA cadence is different for the EUV passbands and UV passbands. It is 24 s for the 1,600 and 1700 passbands, and it is 12 s for the EUV passbands. AIA provides full-disk observation of the Sun in three ultraviolet (UV)-visible channels at 1,600 Å, 1700 Å and 4,500 Å, and seven EUV channels at 171 Å, 193 Å, 211 Å, 94 Å, 304 Å, 335 Å, and 131 Å, respectively. Among the ten different wavelength channels, six wavelengths are at strong iron lines (Fe XI 131Å, FeIX 171Å, FeXII 193Å, FeXIV 211Å, FeXVI 335Å, FeXVIII 94Å) covering the coronal temperature range from T ≈ 0.6 MK to ≳ 16 MK.

3 OBSERVATION AND PLASMA DIAGNOSTICS METHOD

These filters, together, cover a broad temperature range which facilitates the use for the purpose of differential emission measure (DEM) analysis.

All of AIA level 1 data were downloaded from the website of Joint Science Operation Center (JSOC) (http://jsoc.stanford.edu). Then the aia_prep.pro routine in the Solar Software (SSW) package was used to align the AIA Level 1 data to sun-center

and interpolate them to a plate scale of 0.″6 per pixel, the calibrated Level 1.5 data are used in this paper.

For the EUV-UV optically thin lines, the total intensity is defined as

$$I(\lambda) = \frac{1}{4\pi}\int_l Ab\ G(T_e, n_e) n_e n_H dl, \tag{1}$$

where l is the line of sight through the emitting plasma, Ab is the abundance of the element with respect to hydrogen, $G(T_e, n_e)$ is the contribution function that contains all the atomic physics parameters, n_e and T_e are the electron number density and temperature, and n_H is the hydrogen number density. The detailed description can be found in Parenti et al. (2017).

To estimate the distribution of the plasma emission measure and the temperature, the DEM inversion is more appropriate to probe the multi-thermal plasma, when a set of lines from optically thin plasma that formed at different temperatures is available. A DEM distribution gives information about the plasma distribution as a function of temperature along a given line of sight. The DEM is proportional to $n_e n_H$ in the temperature intervals dT_e, and it is given as

$$DEM(T_e) = n_e n_H \frac{dl}{dT_e}. \tag{2}$$

The observed intensity I_λ in wavelength λ can be determined by

$$I_\lambda = \int R_\lambda(T) \times DEM(T) dT, \tag{3}$$

where $R_\lambda(T)$ is the temperature response function of passband λ. **Figure 1** shows the temperature response curves of the six wavelengths (335, 211, 193, 171, 131, 94 Å) with different colors which are obtained from the routine "aia_get_response.pro" in the SSW package. DEM(T) denotes the plasma DEM in the corona, which is computed using the routine "xrt_dem_iterative2.pro". This code was originally designed for processing Hinode/XRT (X-ray Telescope) data (Golub et al., 2004; Weber et al., 2004), and it is modified slightly to work with SDO/AIA data (see also Schmelz et al., 2010).

Based on this DEM method and modified routine, Cheng et al. (2012) derived the DEM profiles of a CME using six dominant iron lines. Later, this method has also been used for temperature diagnostics of solar flares (Yan et al., 2018), recurring jets (Zhang and Ji 2014) and current sheets (Li et al., 2016). Here, logT is set in the range of 5.5–7.5, where the DEM is generally well constrained (Hannah and Kontar 2012; Aschwandern et al., 2013), and $\Delta\log T = 0.1$.

To obtain the emission measure (EM) in the temperature ranges $[T_{min}, T_{max}]$, we evaluate EM using the following equation:

$$EM = \int_{T_{min}}^{T_{max}} DEM(T) dT = \int n_e^2 dh, \tag{4}$$

where n_e denotes the electron number density.

The effective temperature, which is the DEM-weighted average, is calculated by

$$T_{eff} = \frac{\int_{T_{min}}^{T_{max}} DEM(T) T dT}{\int_{T_{min}}^{T_{max}} DEM(T) dT}. \tag{5}$$

4 RESULT

4.1 Introduction of a Jet

A series of jets appeared at the west edge of AR 11 513 on 2012 July 2 (Chen et al., 2015). One of these jets occurred at around 22: 30 UT, and the driving mechanism are studied by Chen et al. (2017). The complex jet went through two phases originating from different magnetic patches. Before 22:29 UT, the jet was in Phase 1; after 22:31 UT, the jet was in Phase 2. The evolution processes of the jet in six different wavelengths are shown in the online animation (**Supplementary Video**). In Phase 1, two blobs appeared in the jet; and in Phase 2, three distinct blobs were clearly shown in the jet. **Figure 2** presents the images obtained by 171 Å for Phase 1 and Phase 2 and the related photospheric magnetogram obtained by HMI. The eruption of the jet originated from magnetic cancellation. Phase 1 was triggered by the magnetic cancellation between p1 and n0, Phase 2 was triggered by the magnetic cancellation between p2 and n0. P1, n1, n0, p2, n2 are marked in **Figure 2C**. Detailed triggering process can be found in Chen et al. (2017).

In order to describe the evolution of the blobs more clearly, we separate the two phases into the following two subsections.

4.2 Two Blobs in Phase 1

In order to identify blobs clearly, we plot the intensity profiles along the spine of the jet in **Figure 2A**, the region which is marked with a white rectangle is selected to calculate the total intensity of the jet spine. **Figure 3** shows the normalized intensity along the jet spine at different moments, 22:27:23, 22:27:59, 22:28:11, 22:28: 35, separately. Here, the minimum intensity between the two peaks in **Figures 3B,C** is considered as the background intensity of the jet, the solid lines in **Figures 3A–D** show this intensity. When the intensity is 1.5 times of the background intensity, the dashed lines are plotted. In **Figures 3B,C**, there are two peaks above the dashed lines with great slopes, through looking at **Figure 2A**, the two bright regions with elliptical shapes, which are called Blob 1 and Blob 2 in phase 1.

The evolution process of two blobs in Phase 1 of the jet is shown in **Figure 4**. In column 1, the evolution of the jet and related blobs appeared in AIA 171 Å. The moments of the 171 Å images in **Figure 4** are the same as the moments in **Figures 3A–D**. Originally, at 22:27:23 UT, a jet appeared and there are some concentrated parts in the jet which can be observed in **Figure 4A**. During the evolution, the jet becomes longer. At 22: 27:59 UT, the jet is almost coherent and there are two regions brighter than other parts of the spire. 12 s later, the two bright regions show clear elliptical shapes, Blob 1 and Blob 2 which are marked in **Figure 4C**. 24 s later, the two blobs disappear and the jet is almost coherent.

Using the DEM method as we described in **Section 2**, EM and DEM-weighted average temperature maps during the evolution

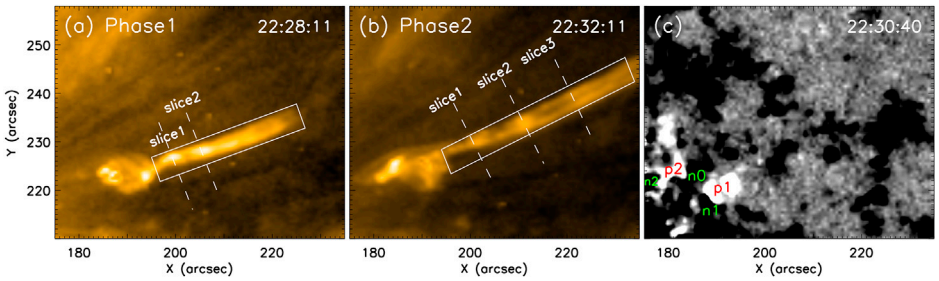

FIGURE 2 | Jet images in two phases obtained from AIA 171 Å and a photospheric line-of-sight magnetogram obtained by HMI. **(A)** and **(B)** 171 Å images show the jet in Phase 1 and Phase 2. **(C)** A related photospheric magnetogram. FOV: 60″ × 48″.

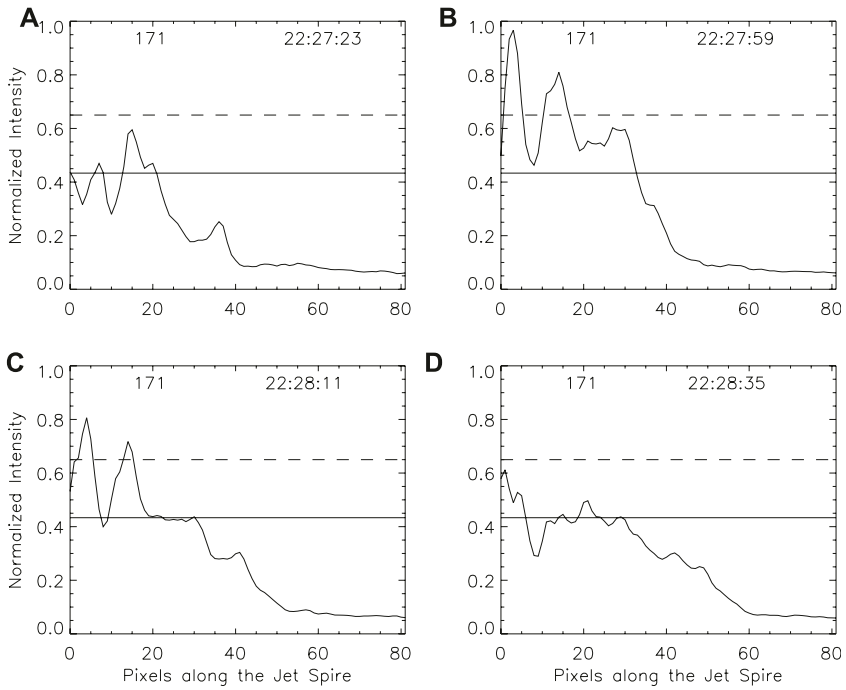

FIGURE 3 | Intensity profiles along the spine of the jet in **Figure 2A**. We select the region which is marked with a white rectangle in **Figure 2A** to calculate the total intensity of the jet spine. The different curve indicates the normalized intensity along the jet spine at different moments, 22:27:23, 22:27:59, 22:28:11, 22:28:35, separately.

of Phase 1 are obtained from the six dominant iron lines (335, 211, 193, 171, 131, 94 Å). Before using this routine, the "aia_bp_estimate_error.pro" function is used to obtain an estimate uncertainty in the measurement, then each image divided by exposure time, the same time period images are obtained. The six images closest in time are selected to derive the EM and DEM-weighted average temperature. The logarithmic distribution of EM during the evolution of the two blobs are plotted in **Figures 4E–H**. In column 2 of **Figure 4**, the EM distribution, as a good proxy, exhibit the variation of the plasma density. The density of the jet originally is concentrated, around 36 s later, it becomes coherent. 12 s later, two blobs appeared. **Figure 4G** shows that the blobs have higher density than the surrounding environment. The logarithmic distribution of DEM-weighted average temperature during the evolution of the Phase 1 are presented in **Figures 4I–L**.

In order to obtain the width of each blob, perpendicular to the jet, we plot an intensity curve along each blob which is shown in **Figure 5A,B**. After subtracting the background intensity, we make a Gaussian fitting for the intensity curve and take the full width at half maximum (FWHM) as the width of the blob. The measured widths of two blobs are shown in **Figure 5 A,B**, the characteristic width of Blob 1 is 1.3 Mm and Blob 2 is 1.5 Mm. DEM method is used to obtain logarithmic DEM curves of the blobs. In order to determine the DEM distribution of the blobs, we construct boxes in **Figure 4C**, and calculate the mean value of the pixels in the boxes. The logarithmic DEM variation at different temperatures of the two blobs are plotted in

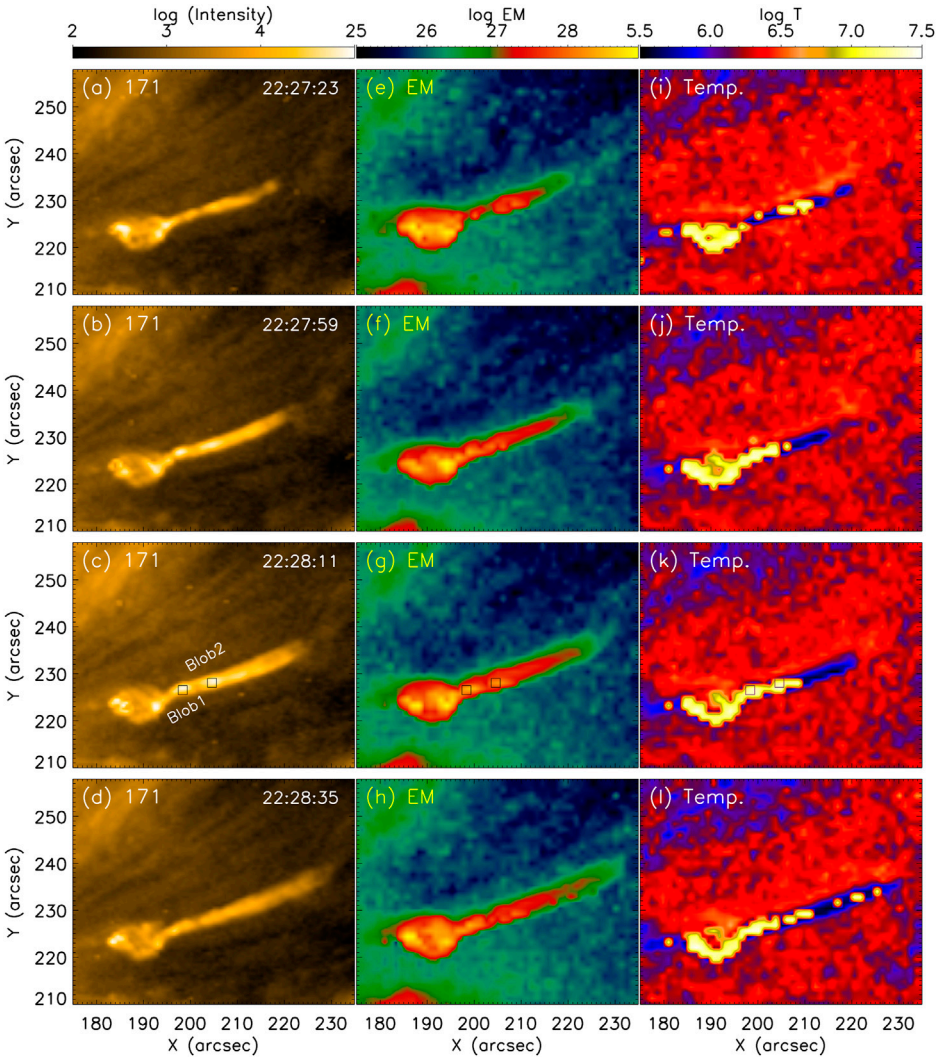

FIGURE 4 | Column 1: evolution of the jet in Phase 1 with the blob formation in 171 Å at three consecutive snapshots with time indicated in the upper right corner in each panel. Column 2: emission measure of the jet at the same time as indicated in column 1. Column 3: DEM-weighted average temperature of the jet at the times as of column 1. FOV: 60″ × 48″.

Figure 5C,D. The effective temperatures of Blob 1 and 2 are 2.66 and 4.00 MK, and the EMs are 5.22 $\times 10^{27}$ and 6.73 $\times$ 10^{27}cm^{-5}. To evaluate the level of uncertainties of the reconstructed DEM curves, 100 Monte Carlo simulations were conducted for each inversion. In **Figure 5C,D**, the red lines stand for the best-fitted DEM curves from the observed values, the black dashed lines represent the reconstructed curves from the 100 MC simulations.

The layout of Phase 1 of the jet at different wavelengths (304 Å, 171 Å, 193 Å, 211 Å, 335 Å, 131 Å) is shown in the animation, through which, we see that the morphology of the jet is similar in the different wavelengths. This means that blobs are multi-thermal structures, they can occur at chromosphere, transition region and corona. Let us now make a wide slit along the jet to determine the properties of the observed EUV blobs (The white box in **Figure 2A** is the slit).

Figure 6 shows the corresponding time-distance plots of the jet. In **Figure 6**, the trajectories of Blob 1 and Blob 2 are not distinct in 171 Å and 131 Å. However, we can see the brightened areas that are moving away from the jet. The trajectory of two blobs in 304 Å is a little clearer. The velocities of the two blobs can be obtained from 304 Å, but with big errors, they are 59 ± 20 km/ s, 98 ± 14 km/ s.

We also made two slits perpendicular to the jet, but along slice 1 and slice 2 (**Figure 2A**). Unfortunately, we can not determine a clear tendency from these plots, therefore we do not show them in the paper.

4.3 Three Blobs in Phase 2

In Phase 2, we plot the intensity profiles along the spine of the jet in **Figure 2B** in order to identify blobs clearly. The region which is marked with a white rectangle is selected to calculate the total intensity of the jet spine. **Figure 7** present the normalized

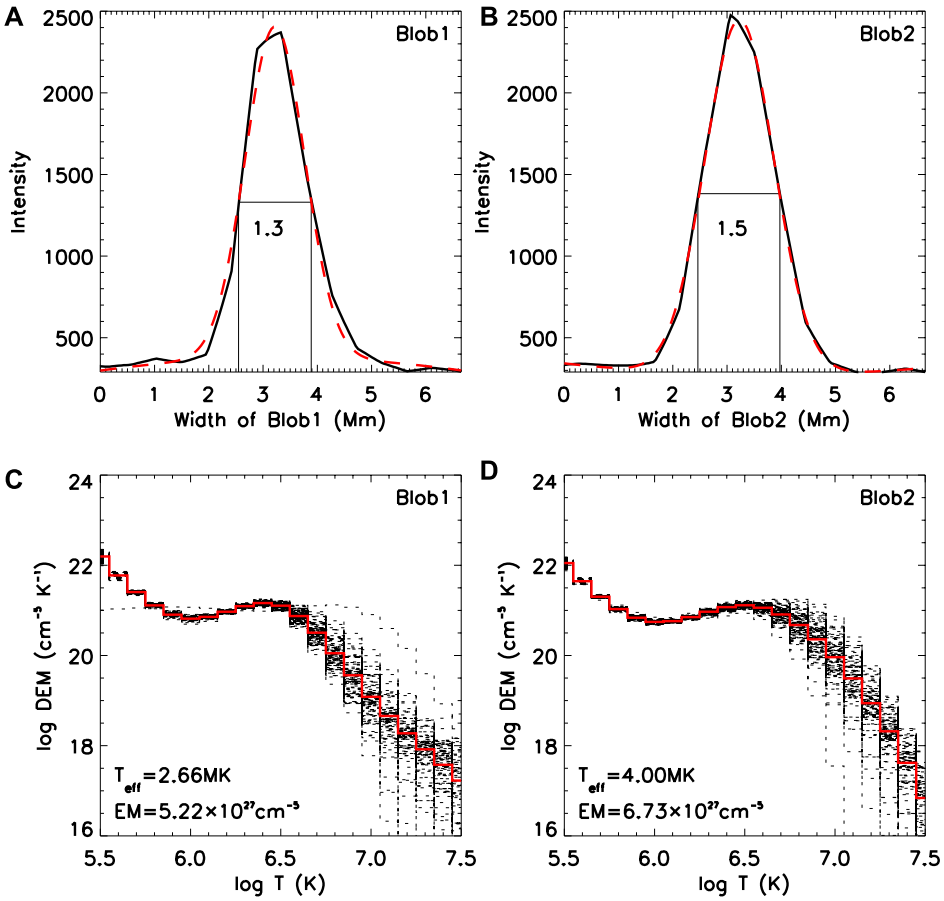

FIGURE 5 | The width (upper panels) and DEM distribution (lower panels) of Blobs 1 and 2 in Phase 1. In **(A)** and **(B)**: the black solid curves are the intensity variation of the Blobs 1 and 2 perpendicular to the jet; the red dashed lines are Gaussian fitting with the width values taken at the full width of half maximum (FWHM) after subtracting the background intensity values. **(C)** and **(D)** show the DEM profiles of the core regions in Blobs 1 and 2; the red solid lines stand for the best-fitted DEM curves from the observed values; the black lines represent the reconstructed curves from the 100 MC simulations.

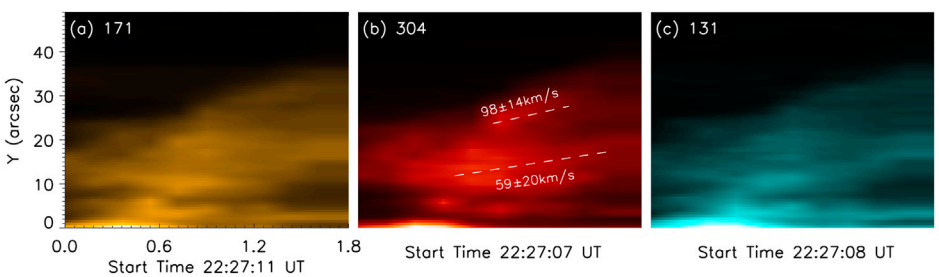

FIGURE 6 | Time-distance plots of the blobs along the jet shown in **Figure 4B** at three different wavelengths: 171Å, 304 Å and 131 Å.

intensity along the jet spine at different moments, 22:31:11, 22:32:11, 22:32:23, 22:32:59, separately. Here, the minimum intensity between the three peaks in **Figures 7B,C** is considered as the background intensity of the jet, the solid lines in **Figures 7A–D** show this intensity. When the intensity is 1.5 times of the background intensity, the dashed lines are plotted. In **Figure 7B**, there are three peaks above the dashed lines with great slopes, through looking at **Figure 2B**, the three bright regions with elliptical shapes, which are called Blob 1, Blob 2 and Blob 3 in phase 2.

Snapshots capturing stages of the evolution in Phase 2 of the jet, the associated logarithmic distribution of emission measure (EM) and temperature in Phase 2 are shown in **Figure 8**. The EM and temperature distributions are obtained using the same

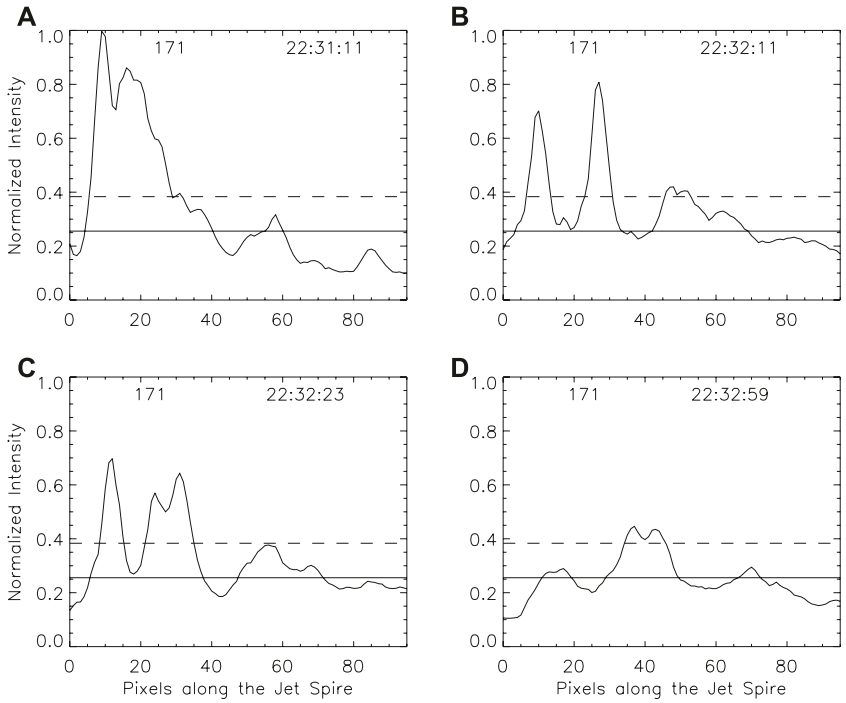

FIGURE 7 | Intensity profiles along the spine of the jet in **Figure 2B**. We select the region which is marked with a white rectangle in **Figure 2B** to calculate the total intensity of the jet spine. The different curve indicates the normalized intensity along the jet spine at different moments, **(A)** 22:31:11, **(B)** 22:32:11, **(C)** 22:32:23, **(D)** 22:32:59, separately.

method described in **Section 3**. In the first column, four stages of the evolution of the jet are depicted in 171 Å. Note the very rapid formation from 22:31:11 UT to 22:32:59 UT. In the second column, the corresponding emission measure maps are shown, while in the third column, the associated temperature maps are depicted. At 22:31:11 UT, the intensity of the jet is coherent and bright (**Figure 8A**). The emission measure of the jet (**Figure 8E**) is separated at the bottom and top parts: at the bottom part, the EM is strong; and at the top part, the EM is somewhat weaker. The temperature of the jet (**Figure 8I**) is dominant in the first snapshot. A minute later, at 22:32:11 UT, the intensity of the jet became discrete and rather fragmented. There appear three bright and compact patches (**Figure 8B**), labelled as Blob 1, Blob 2 and Blob 3. Between the blobs, the intensity became even weaker than before as if plasma had been evacuated suddenly. The EM and temperature of the jet (**Figures 8F,J**) have also evolved accordingly. There are three strong patches identifiable in EM and temperature which correspond spatially well to the locations to Blobs 1-3 in the intensity distributions (**Figure 8B**). Between the highlighted patches, again, the regions became weaker. A further 12 s later, the blobs including their EM and temperature became rather diffuse. By 22:32:59 UT, the blobs disappear almost entirely. Therefore we conclude that the lifetime of these blobs is about 50 s.

In order to obtain an insight into the intensity variation of the jet during the evolution of the blobs, we choose one part of the jet and determine the normalized intensity variation of that partition at six wavelengths (304 Å, 171 Å, 193 Å, 211 Å, 335 Å, 131 Å). The part is almost at the root of the jet which are marked by a white-color box in the top-right panel of **Figure 9**. The normalized intensity variation of the part in the white-color box in six wavelengths are also plotted in **Figure 9**. The six curves depict that the intensity is decreasing during the evolution of the jet. After 22:33 UT, the intensity is only about a third of the maximum intensity. The tendency is almost the same in different wavelengths indicating that the intensity variation occurs from the chromosphere, through the transition region and also in the corona.

The measured width, the logarithmic DEM distribution of the blobs are presented in **Figure 10**. Perpendicular to the jet and along the blobs, we plot the intensity distribution. After subtracting the background intensity, we make a Gaussian fitting and determine the full width of half maximum (FWHM) as the characteristic width (or diameter) of the blob. We found that the width of Blob 1 is 1.4 Mm, Blob 2 is 2.3 Mm. From **Figure 8B**, we can also see that there are two branches along Blob 3, so there are two peaks in the intensity diagram (**Figure 10C**). We estimate the width of Blob 3 as 0.8 Mm. In order to determine the EM and temperature of blobs, we construct boxes in **Figure 8B**, and calculate the average values of the pixels in the boxes. The effective temperatures of Blobs 1, 2 and 3 are 2.34, 2.32 and 2.12 MK, respectively. The mean EMs of the blobs are 5.04×10^{27} cm^{-5}, 5.98×10^{27} cm^{-5} and 2.26×10^{27} cm^{-5}, respectively.

Let us now fit a wide slit along the jet to determine some of the properties of the observed EUV blobs (**Figure 2B**).

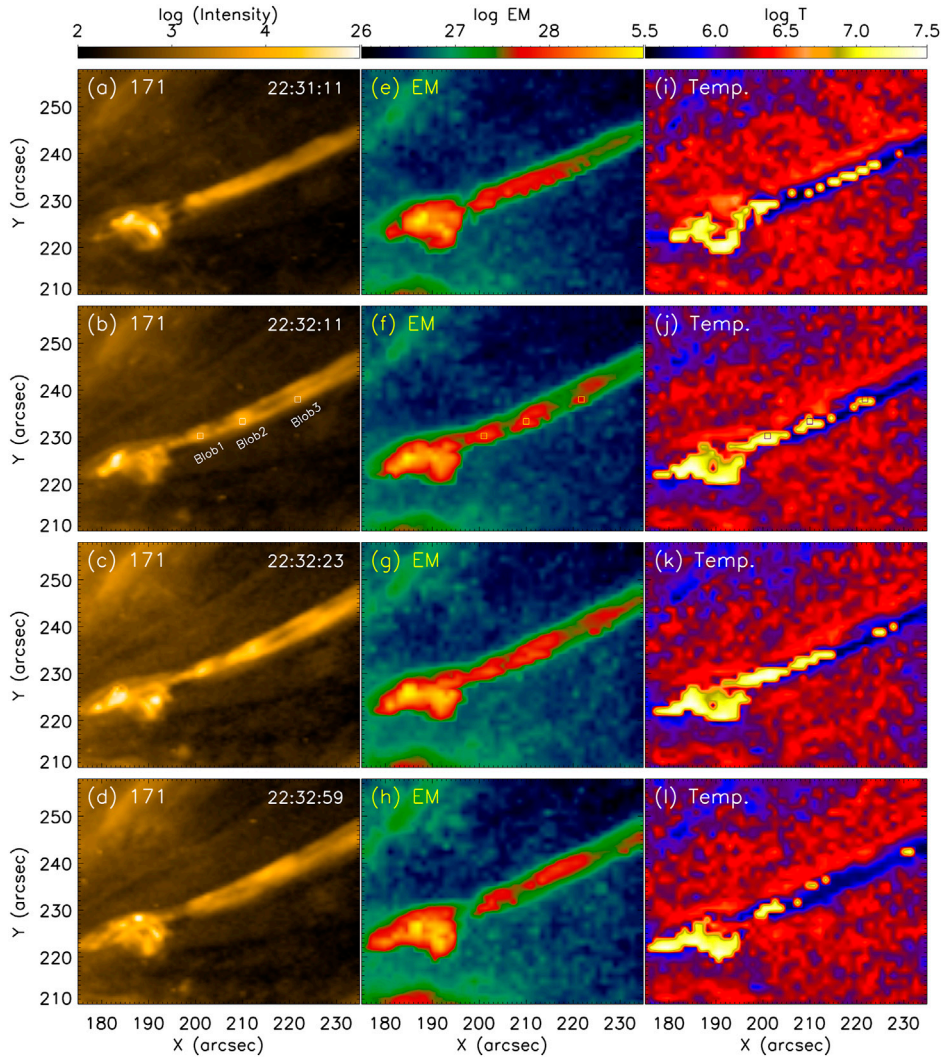

FIGURE 8 | Column 1: evolution of the jet in Phase 2 with the blob formation in 171 Å at four consecutive snapshots with time indicated in the upper right corner in each panel. Column 2: emission measure of Phase 2 at the same time as indicated in column 1. Column 3: temperature of Phase 2 at the times as of column 1. FOV: 60″ × 48″.

The corresponding time-distance images are shown in **Figure 11** at three wavelengths. In 171 Å, 304 Å, 131 Å, each time-distance plot have three trajectories, which indicates that the three blobs have different velocities. We now determine the velocities of the three blobs in 171 Å. White dashed lines are plotted in **Figure 11A** represent the trajectories of the three blobs. The velocities of the blobs can be obtained, they are 94 ± 5 km s^{-1}, 128 ± 10 km s^{-1} and 185 ± 8 km s^{-1}.

In order to have some insight into the evolution of each blob, we make three slice cuts perpendicular to the jet. The time-distance images of the three slices are presented in **Figure 12**. In the first (second, third) row, the evolution of Blob 1 (2, 3) is demonstrated. In the three columns, the evolution of the blobs are captured at different wavelengths 171 Å, 304 Å, 131 Å. Along Slice 1, in **Figures 12A,D,G**, we note that there is a bright patch at the beginning, then the bright patch became weaker; around a minute later, another bright patch appeared, i.e. Blob 1 which is shown in **Figures 2B**, **8B**. Along Slice 2, in **Figures 12B,E,H**, there is also a bright patch at the beginning, then it became weaker; more than a minute later, another bright patch appeared, what is Blob 2. The evolution processes of Blob 1 and Blob 2 are almost identical: initially, there is a bright patch, then the intensity became weaker, followed by about a minute later, it became bright again, and we can identify clear blob structures at 22:32: 11 UT. Along Slice 3, in **Figures 12C,F,I**, at the beginning, we see that there is some brightness, what became weaker. Later, there are two small bright patches. In columns 1, 2 and 3 of **Figure 12**, the entire evolution processes are demonstrated and found to be similar at the three different wavelengths for the three slices.

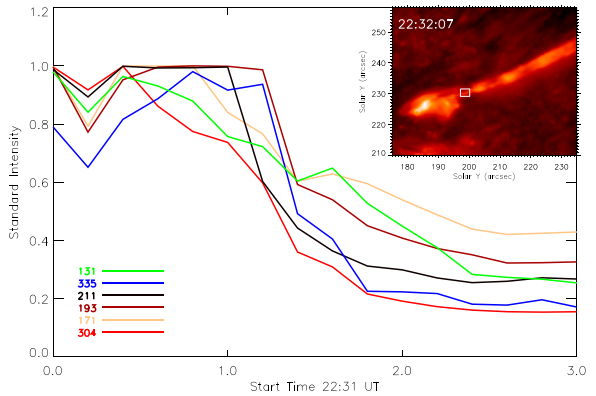

FIGURE 9 | Normalized intensity variation of a part of the jet in Phase 2 in six different wavelengths (304 Å, 171 Å, 193 Å, 211 Å, 335 Å, 131 Å). Top-right: An image of the jet in Phase 2 with three blobs obtained from SDO/AIA 304 Å at 22:32:07 UT, the white-color box marks the region that we calculate the intensity variation.

4.4 Summary for the Two Phases

The evolution of the jet resembles a process that magnetized plasma has at a reconnection site and filling the jet: the emission of the plasma causes the jet becoming brighter, the hot plasma moves away from the jet and the jet become weaker. The main observational results can be summarized as follows.

In Phase 1, two blobs were observed simultaneously in different wavelengths (304 Å, 171 Å, 193 Å, 211 Å, 335 Å, 131 Å), i.e. the two blobs appeared at the same time. It is not one blob appeared, then another blob appeared in succession, they did not appear intermittently. In Phase 2, three blobs were also observed simultaneously which is the same as in Phase 1. Our result is different from Zhang and Ji. (2014). In their observation, they found blobs in recurring jets, but only one blob in one jet: firstly, they observes a blob in a jet, then they observed another blob in the next jet, later they observed the third blob in the following jet. The jets recurred three times with an interval of 40–45 min.

All of the blobs were observed at the jet spire, not at the base of the jet. As we know, the jet is formed due to magnetic reconnection between the closed magnetic field and open magnetic field. The magnetic reconnection region located at the base of jet. Singh et al. (2012) observed blobs in the chromosphere both at the jet spire and at the base of the jet. But they only found one blob at the jet spire and one blob at the base of the jet.

The intensity of the other partitions of the jet was increased when the two blobs appeared (**Figure 4A–C**) in Phase 1. The EM and temperature were also increased (**Figure 4E–G, I–K**) during the evolution of the jet. The intensity, EM and temperature of the other partitions of the jet were decreased when the three blobs appeared (**Figure 8**) in Phase 2. In order to know how the intensity varies in the jet, we took one partition of the jet in Phase 2 and plotted the standard intensity variation of this partition in six different wavelengths (304 Å, 171 Å, 193 Å, 211 Å, 335 Å, 131 Å) and found that the intensity decreased to one third of the original intensity at the end (**Figure 9**).

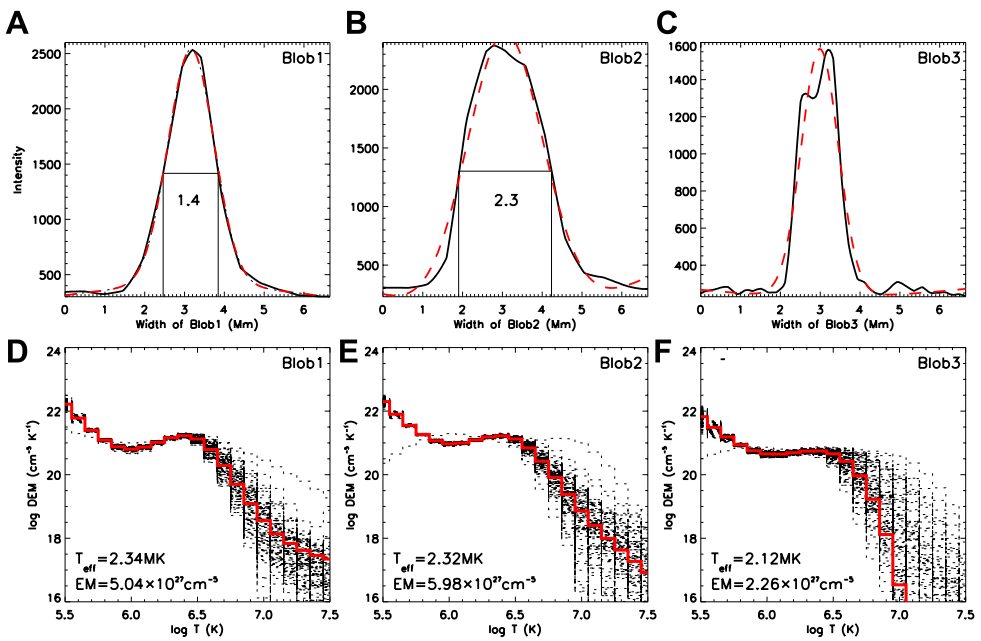

FIGURE 10 | The width (upper panels) and DEM distribution (lower panels) of Blobs 1, 2 and 3 in Phase 2. In **(A)**, **(B)**, and **(C)**: the black solid curves are the intensity variation of the Blobs 1, 2 and 3 perpendicular to the jet; the red dashed lines are Gaussian fitting with the width values taken at the full width of half maximum (FWHM) after subtracting the background intensity values. **(D)**, **(E)**, and **(F)** show the DEM profiles of the core regions in Blobs 1, 2 and 3; the red solid lines stand for the best-fitted DEM curves from the observed values; the black lines represent the reconstructed curves from the 100 MC simulations.

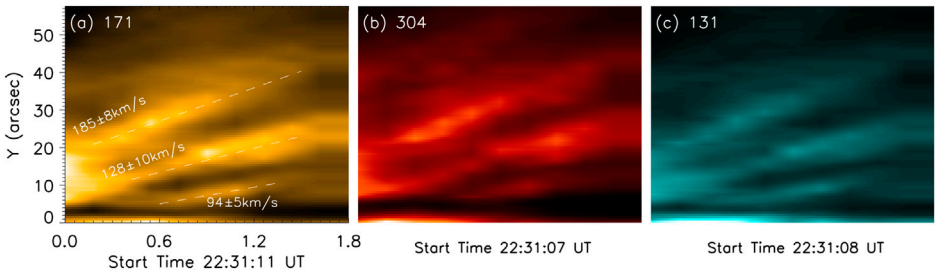

FIGURE 11 | Time-distance plots of the blobs along the jet shown in **Figure 2B** at three different wavelengths: 171Å, 304 Å and 131 Å.

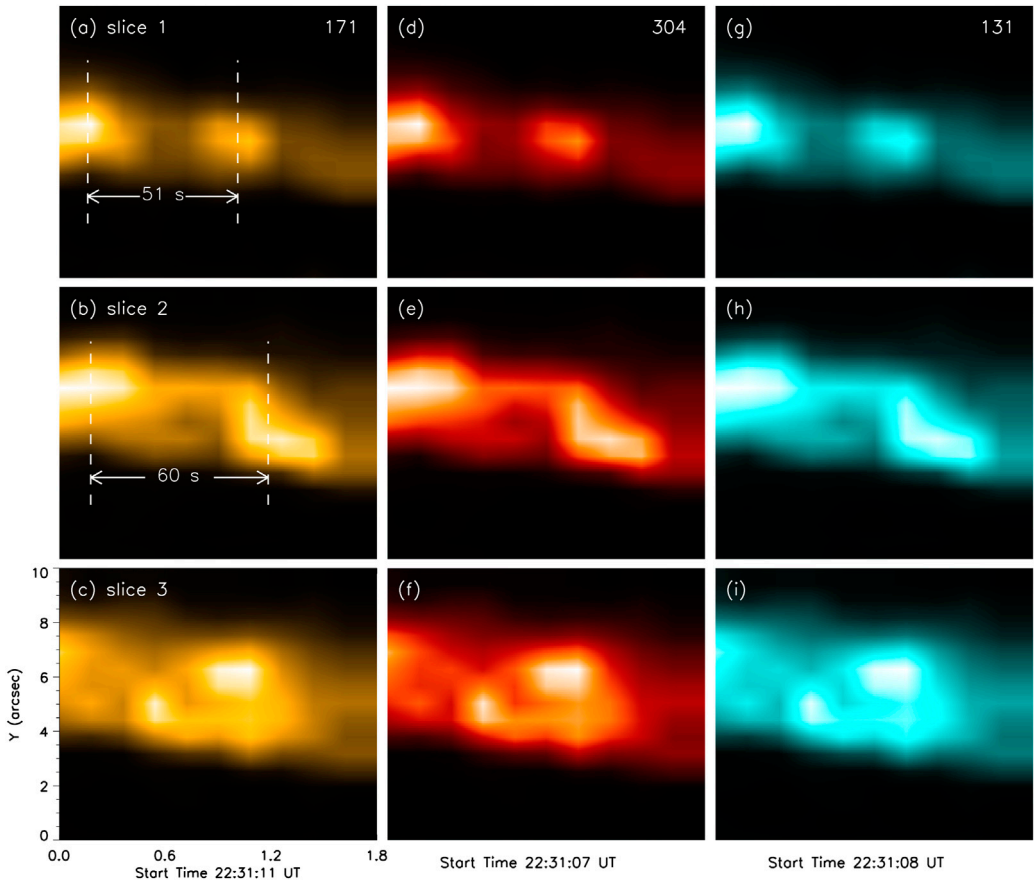

FIGURE 12 | Time-distance images of the blobs along the white dashed lines, i.e., perpendicular to the axis of the jet, as shown in **Figure 9B** at three different wavelengths: 171 Å, 304 Å and 131 Å.

The widths of the blobs are obtained using Gaussian Fitting. In Phase 1, the widths of the two blobs are 1.3 and 1.5 Mm; in Phase 2, the widths of the blobs are 0.8, 1.4, 2.3 Mm. Blobs appeared in different wavelengths, they are multi-thermal in nature. Using DEM method, we can get the EM values of blobs, and we can get effective temperatures of blobs. The EM values of the blobs is 2–7 $\times 10^{27} cm^{-5}$, the effective temperature of the blobs is 2–4 Mk, which is comparable to the values of the blobs obtained by Zhang and Ji. (2014).

Velocities of the blobs were calculated through time-distance plots. Velocities of the two blobs in Phase 1 are 59 ± 20 km/ s and 98 ± 14 km/ s. The blob close to the base of the jet had lower velocity than the other. Velocities of the three blobs in Phase 2 are 94 ± 5 km/ s, 128 ± 10 km/ s and 185 ± 8 km/ s. From the base of the jet to the top of the jet spire, blobs located at higher projected altitudes, blobs owned larger velocities. The three blobs in Phase 2 have different velocities which may be accounted for the untwisting of the jet, where the evolving magnetic pressure

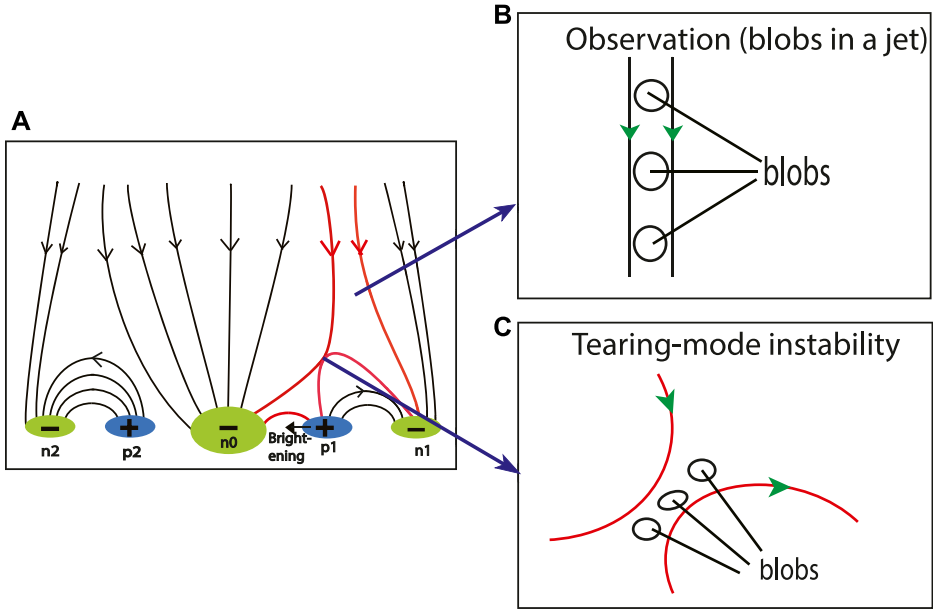

FIGURE 13 | (A) A magnetic schematic diagram of the jet, **(B)** a cartoon shows the observational blobs in the jet, **(C)** a cartoon shows the blobs in tearing-mode instability.

causes the different blobs velocities. Here the increased velocities refer to the different blobs at different time instants.

Chae et al. (2017) and Patel et al. (2020) studied blobs associated with post-CME current sheets. In Chae et al. (2017)'s study, they found the six blobs have a mean speed around 303 km/s at the heights from 2.5 to 14 R$_\odot$. In Patel et al. (2020)'s study, they found that downward- and upward-moving blobs have average speeds of ~272 km/ s and ~191 km/ s in the EUV observation, the average speed of blobs increased to ~671 km/ s and ~1,080 km/ s in the K-Cor and LASCO/C2 observations. There results show that the blobs velocity became bigger and bigger from the base of the Sun to the higher layer of the Sun. Patel et al. (2020)'s result presents the upward-moving blobs have an average speed 191 km/ s in the EUV observation which are comparable to the velocity of Blob 3 in Phase 2 in our case.

Two blobs in Phase 2 appeared periodicity in different wavelengths (**Figure 12**). In the three blobs of Phase 2, there are two blobs, first appeared, then disappeared, later appeared again, finally disappeared; i.e. each blob appeared twice at the same location. The period of the two blobs has a little difference, the period is 51 s for Blob 1, and it is 60 s for Blob 2.

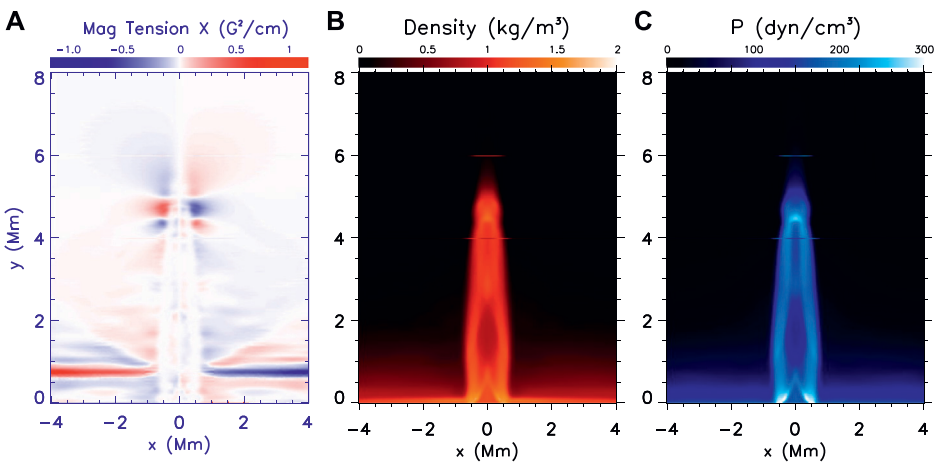

FIGURE 14 | The results of a numerical simulation studying the morphology of a jet in a stratified solar atmosphere with a vertical uniform magnetic field. **(A)**: distribution of magnetic tension; **(B)**: density; **(C)**: pressure.

5 CONCLUSION AND DISCUSSION

A complex jet located at the west edge of AR 11 513 occurring at around 22:30 UT on 2012 July 2 was analyzed. There are two phases of the jet, which were originated from photosphric magnetic cancellation. Two blobs were observed in Phase 1 and three blobs were clearly observed along the EUV jet in Phase 2. The formation and evolution processes of multi-blobs in a single jet were studied.

One mechanism that may be responsible for the blob-like structures is tearing-mode instability (TMI). In magnetic reconnection theory, a current sheet in an antiparallel magnetic field is unstable which can create blob-like structures due to TMI (Furth et al., 1963). For this complex jet, two phases were originated from photospheric magnetic cancellation. Considering Phase 1, the magnetic cancellation between P1 and n0 induces magnetic reconnection in the upper layer occurring at open magnetic field lines and closed magnetic field lines. There are opposite directions for the open magnetic lines originating from n0 and closed magnetic lines originated from p1. A schematic diagram of the topology and magnetic reconnection is shown in **Figure 13A**, which is taken from **Figure 7C** in the paper of Chen et al. (2017).

In both of two phases, multi-blobs were observed in a single jet spine; at the jet base, there were also brighting structures with elliptical shapes. The velocities of the blobs in the jet spine increases from the lower part to the upper part. These observations provide pivotal evidence for the TMI. Schematic diagrams of the jet and blobs are shown in **Figure 13**. Blobs are observed at jet in unidirectional magnetic fields, the detailed region is shown in **Figure 13A** and the configuration is shown in **Figure 13B**. If TMI create blobs, the blobs should be formed in magnetic reconnection region with antiparallel magnetic fields. The detailed region of the blobs created by TMI is shown in **Figure 13A** and the magnetic configuration is shown in **Figure 13C**. One possible explanation for the blobs formation is: several blobs are created at magnetic reconnection region (the base of jet) due to TMI, which escape from that location to the jet.

In the solar corona, cylindrical geometry of coronal loops is a very popular geometry enabling us a first insight into the local plasma dynamics. In such a plasma, current pinch instabilities represent an important class of magnetohydrodynamics (MHD) instabilities, such as the kink or sausage mode instability. For cylindrical magnetic flux tubes, the kink-unstable mode ($m = 1$ mode, where m is the azimuthal wavenumber) is observed frequently (e.g., Vemareddy and Zhang 2014; Yang et al., 2016). However, an equally plausible another type of instability, known as sausage mode ($m = 0$) instability, was only reported recently by Srivastava et al. (2013) during a prominence eruption recorded on September 12, 2011 by AIA onboard SDO. For the sausage instability, the diameter of the flux tube should have an obvious difference in different parts. Here, there is not observational evidence showing the obvious different diameters along the jet.

In order to see whether blobs can be formed in jets, we carry out simple simulations. The jet is driven with a Gaussian momentum pulse for 300 S with a width of 350 km near the photosphere. The simulated jet was created using the open source MPI-AMRVAC software version 2.0 (Zhang and Zhang, 2017). **Figure 14** displays the numerical simulation results studying the morphology of a jet in a stratified solar atmosphere with a vertical uniform magnetic field. The detailed description of the method can be found in Mackenzie Dover et al. (2020, 2021). We set the domain size to 50 Mm × 30 Mm with a level one resolution of 32 × 24 (giving a physical resolution of 1.56 Mm × 1.25 Mm). This coarse level one resolution was chosen to allow the dissipation of shocks as they travel towards the boundaries. To capture the internal structure of the jet we applied 7 levels of AMR giving a spatial resolution of 12 km × 10 km. We use unidirectional grid stretching in the horizontal direction, where from the origin grid cells change by a constant factor of 1.1 from cell to cell. Similarly to observed jet, the simulated jet has formed knots along the central the axis of the jet. The initial magneto-hydrostatics stratification places the TR at 2 Mm where the temperature smoothly links 8000 K chromosphere to a 1.8 MK corona.

DATA AVAILABILITY STATEMENT

The original contributions presented in the study are included in the article/**Supplementary Materials**, further inquiries can be directed to the corresponding author.

AUTHOR CONTRIBUTIONS

JC, RE, JL YD, MZ, and JS contributed to the conception and design of the study. JC performed the most data analysis and wrote the first draft of the manuscript. FD, QZ, and LL performed parts of the data analysis. All authors contributed to manuscript revision, read and approved the submitted version.

FUNDING

This work was supported by the China-Hungary Exchange Program, CAS. This work was also supported by the Strategic Priority Research Program on Space Science, the Chinese Academy of Sciences, Grant No. XDA15320302, XDA15052200, XDA15320102. This work was partly supported by the National Natural Science Foundation of China (Grant nrs. 11973056, 11773038, U1831107).

ACKNOWLEDGMENTS

We thank the discussion with Jun Lin, D. Banerjee. SDO is a mission for NASA's Living With a Star program. RE thanks the Science and Technology Facilities Council (STFC, UK) for the support received and is also grateful to International Mobility

Scheme of the University of Sheffield, UK. RE also acknowledges the support received by the Chinese Academy of Sciences Presidents International Fellowship Initiative, Grant No. 2016VMA045, and the warm hospitality received at NAOC of CAS, Beijing, where part of his contribution was made.

SUPPLEMENTARY MATERIAL

The Supplementary Material for this article can be found online at: https://www.frontiersin.org/articles/10.3389/fspas.2021.786856/full#supplementary-material

REFERENCES

Asai, A., Ishii, T. T., and Kurokawa, H. 2001, Plasma Ejections from a Light Bridge in a Sunspot Umbra, 555, L65, L68. doi:10.1086/321738

Aschwanden, M. J. (2004). *Physics of the Solar Corona: An Introduction*. Chichester, UK: Praxis Publishing Ltd., P270.

Aschwandern, M. J., Boerner, P., Schrijver, C. J., and Malanushenko, A. (2013). *SoPh* 283, 5.

Beckers, J. M. (1968). *Solar Spicules (Invited Review Paper)*, 3, 367. doi:10.1007/bf00171614

Borrero, J. M., Tomczyk, S., Kubo, M., Socas-Navarro, H., Schou, J., Couvidat, S., et al. (2011). VFISV: Very Fast Inversion of the Stokes Vector for the Helioseismic and Magnetic Imager. *Sol. Phys.* 273, 267–293. doi:10.1007/s11207-010-9515-6

Canfield, R. C., Reardon, K. P., Leka, K. D., Shibata, K., Yokoyama, T., and Shimojo, M. (1996). H Alpha Surges and X-Ray Jets in AR 7260. *ApJ* 464, 1016. doi:10.1086/177389

Chae, J., Cho, K., Kwon, R.-Y., and Lim, E.-K. (2017). Evidence for a Magnetic Reconnection Origin of Plasma Outflows along Post-CME Rays. *ApJ* 841, 49. doi:10.3847/1538-4357/aa6d7a

Chen, J., Su, J., Deng, Y., and Priest, E. R. (2017). A Complex Solar Coronal Jet with Two Phases. *ApJ* 840, 54. doi:10.3847/1538-4357/aa6c59

Chen, J., Su, J., Yin, Z., Priya, T., Zhang, H., Liu, J., et al. (2015). Recurrent Solar Jets Induced by a Satellite Spot and Moving Magnetic Features. *ApJ*, 815, 71.

Cheng, X., Li, Y., Wan, L. F., Ding, M. D., Chen, P. F., Zhang, J., et al. (2018). Observations of Turbulent Magnetic Reconnection within a Solar Current Sheet. *ApJ* 866, 64. doi:10.3847/1538-4357/aadd16

Cheng, X., Zhang, J., Saar, S. H., and Ding, M. D. (2012). Differential Emission Measure Analysis of Multiple Structural Components of Coronal Mass Ejections in the Inner Corona. *ApJ* 761, 62. doi:10.1088/0004-637x/761/1/62

Cirtain, J. W., Golub, L., Lundquist, L., van Ballegooijen, A., Savcheva, A., Shimojo, M., et al. (2007). Evidence for Alfve´n Waves in Solar X-ray Jets. *Science* 318, 1580–1582. doi:10.1126/science.1147050

De Pontieu, B., Erdélyi, R., and James, S. P. (2004). Solar Chromospheric Spicules from the Leakage of Photospheric Oscillations and Flows. *Nature* 430, 536–539. doi:10.1038/nature02749

Furth, H. P., Killeen, J., and Rosenbluth, M. N. (1963). Finite-Resistivity Instabilities of a Sheet Pinch. *Phys. Fluids* 6, 459. doi:10.1063/1.1706761

Golub, L., Deluca, E. E., Sette, A., and Weber, M. (2004). "ASP Conf. Ser. 325," in *The Solar-B Mission and the Forefront of Solar Physics*. Editors T. Sakurai and T. Sekii (San Francisco, CA: ASP), 217.

Hannah, I. G., and Kontar, E. P. (2012). *A&A* 539, 146. doi:10.1051/0004-6361/201117576

Hong, J., Jiang, Y., Yang, J., Yang, B., Xu, J., and Xiang, Y. (2016). Mini-filament Eruption as the Initiation of a Jet along Coronal Loops. *ApJ*, 830, 60.

Hong, J., Jiang, Y., Yang, J., Li, H., and Xu, Z. (2017). Minifilament Eruption as the Source of a Blowout Jet, C-Class Flare, and Type-Iii Radio Burst. *ApJ* 835, 35. doi:10.3847/1538-4357/835/1/35

Huang, Z., Madjarska, M. S., Doyle, J. G., and Lamb, D. A. (2012). Coronal Hole Boundaries at Small Scales - IV. SOT View. Magnetic Field Properties of Small-Scale Transient Brightenings in Coronal Holes. *A&A* 548, 62. doi:10.1051/0004-6361/201220079

Innes, D. E., Bučík, R., Guo, L.-J., and Nitta, N. (2016). Observations of Solar X-ray and EUV Jets and Their Related Phenomena. *Astron. Nachr.* 337, 1024–1032. doi:10.1002/asna.201612428

Kayshap, P., Srivastava, A. K., Murawski, K., and Tripathi, D. (2013). Origin of Macrospicule and Jet in Polar Corona by a Small-Scale Kinked Flux Tube. *Astrophysical J.* 770, 3. doi:10.1088/2041-8205/770/1/l3

Kiss, T. S., Gyenge, N., and Erdélyi, R. (2017). Systematic Variations of Macrospicule Properties Observed Bysdo/aia over Half a Decade. *ApJ* 835, 47. doi:10.1088/1361-6528/aa5272

Kliem, B., Karlický, M., and Benz, A. O. (2000). *A&A* 360, 715.

Kumar, P., Karpen, J. T., Antiochos, S. K., Wyper, P. F., and DeVore, C. R. (2019). First Detection of Plasmoids from Breakout Reconnection on the Sun. *Astrophysical J.* 885, 15. doi:10.3847/2041-8213/ab45f9

Lemen, J. R., Title, A. M., Akin, D. J., Akin, D., Boerner, P., Chou, C., et al. (2012). *SoPh* 275, 17.

Li, L. P., Zhang, J., Li, T., Yang, S. H., and Zhang, Y. Z. (2012). *A&A*, 539A7.

Li, L., Zhang, J., Peter, H., Priest, E., Chen, H., Guo, L., et al. (2016). Magnetic Reconnection between a Solar Filament and Nearby Coronal Loops. *Nat. Phys* 12, 847–851. doi:10.1038/nphys3768

Lin, J., Ko, Y. K., Sui, L., Raymond, J. C., Stenborg, G. A., Jiang, Y., et al. (2005). Direct Observations of the Magnetic Reconnection Site of an Eruption on 2003 November 18. *ApJ* 622, 1251–1264. doi:10.1086/428110

Liu, J. J., Erdélyi, R., Wang, Y., and Liu, R. (2018). *Rui* 852, 10.

Liu, J. J., Fang, F., Wang, Y. M., McIntosh, S., Fang, Y., Zhang, Q., et al. (2016a), 817, 126.

Liu, J. J., Wang, Y. M., Erdélyi, R., Liu, R., McIntosh, S., Gou, T., et al. (2016b). *ApJ*, 833, 150.

Liu, Y., and Kurokawa, H. (2004). On a Surge: Properties of an Emerging Flux Region. *ApJ* 610, 1136–1147. doi:10.1086/421715

Liu, Y., Luhmann, J. G., Lin, R. P., Bale, S. D., Vourlidas, A., Petrie, G., et al. (2009). *ApJ*, L51, 698.

Moore, R. L., Cirtain, J. W., Sterling, A. C., and Falconer, D. A. (2010). Dichotomy of Solar Coronal Jets: Standard Jets and Blowout Jets. *ApJ* 720, 757–770. doi:10.1088/0004-637x/720/1/757

Morita, S., Shibata, K., Ueno, S., Ichimoto, K., Kitai, R., and Otsuji, K.-i. (2010). Observations of Chromospheric Anemone Jets with Hinode Ca II Broadband Filtergraph and Hida Ca II Spectroheliograph. *Publ. Astron. Soc. Jpn.* 62, 901–920. doi:10.1093/pasj/62.4.901

Morton, R. (2012). Chromospheric Jets Around the Edges of Sunspots. *A&A* 543, 6. doi:10.1051/0004-6361/201219137

Morton, R. J., Srivastava, A. K., and Erdélyi, R. (2012). Observations of Quasi-Periodic Phenomena Associated with a Large Blowout Solar Jet. *A&A* 542, 70. doi:10.1051/0004-6361/201117218

Ni, L., Kliem, B., Lin, J., and Wu, N. (2015). Fast Magnetic Reconnection in the Solar Chromosphere Mediated by the Plasmoid Instability. *ApJ* 799, 79. doi:10.1088/0004-637x/799/1/79

Ni, L., Zhang, Q.-M., Murphy, N. A., and Lin, J. (2017). Blob Formation and Ejection in Coronal Jets Due to the Plasmoid and Kelvin-Helmholtz Instabilities. *ApJ* 841, 27. doi:10.3847/1538-4357/aa6ffe

Patel, R., Pant, V., Chandrashekhar, K., and Banerjee, D. (2020). A Statistical Study of Plasmoids Associated with a post-CME Current Sheet. *A&A* 644, 158. doi:10.1051/0004-6361/202039000

Raouafi, N. E., Patsourakos, S., Pariat, E., Young, P. R., Sterling, A. C., Savcheva, A., et al. (2016). Solar Coronal Jets: Observations, Theory, and Modeling. *Space Sci. Rev.* 201, 1–53. doi:10.1007/s11214-016-0260-5

Sarkar, S., Pant, V., Srivastava, A. K., and Banerjee, D. (2016). Transverse Oscillations in a Coronal Loop Triggered by a Jet. *Sol. Phys.* 291, 3269–3288. doi:10.1007/s11207-016-1019-6

Schmelz, J. T., Saar, S. H., Nasraoui, K., Kashyap, V. L., Weber, M. A., DeLuca, E. E., et al. (2010). Multi-stranded and Multi-thermal Solar Coronal Loops: Evidence Fromhinodex-ray Telescope and Euv Imaging Spectrometer Data. *ApJ* 723, 1180–1187. doi:10.1088/0004-637x/723/2/1180

Schmieder, B., Shibata, K., van Driel-Gesztelyi, L., and Freeland, S. (1995). Hα Surges and Associated Soft X-ray Loops. *Sol. Phys.* 156, 245–264. doi:10.1007/bf00670226

Scullion, E., Erdélyi, R., Fedun, V., and Doyle, J. G. (2011). The Response of a Three-Dimensional Solar Atmosphere to Wave-Driven Jets. *ApJ* 743, 14. doi:10.1088/0004-637x/743/1/14

Scullion, E., Popescu, M. D., Banerjee, D., Doyle, J. G., and Erdélyi, R. (2009). Jets in Polar Coronal Holes. *ApJ* 704, 1385–1395. doi:10.1088/0004-637x/704/2/1385

Shen, Y., Liu, Y., Su, J., and Deng, Y. (2012). On a Coronal Blowout Jet: the First Observation of a Simultaneously Produced Bubble-like Cme and a Jet-like Cme in a Solar Event. *ApJ* 745, 164. doi:10.1088/0004-637x/745/2/164

Shen, Y., Liu, Y., Su, J., and Ibrahim, A. (2011). Kinematics and Fine Structure of an Unwinding Polar Jet Observed by the Solar Dynamic Observatory/Atmospheric Imaging Assembly. *ApJ* 735, L43. doi:10.1088/2041-8205/735/2/l43

Shen, Y. (2021). Observation and Modelling of Solar Jets. *Proc. R. Soc. A.* 477, 20200217. doi:10.1098/rspa.2020.0217

Shibata, K., Ishido, Y., Acton, L. W., Strong, K., Hirayama, T., Uchida, Y., et al. (1992). *PASJ* 44, 173.

Singh, K. A. P., Isobe, H., Nishizuka, N., Nishida, K., and Shibata, K. (2012). Multiple Plasma Ejections and Intermittent Nature of Magnetic Reconnection in Solar Chromospheric Anemone Jets. *ApJ* 759, 33. doi:10.1088/0004-637x/759/1/33

Srivastava, A. K., Erdélyi, R., Tripathi, D., Fedun, V., Joshi, N. C., and Kayshap, P. (2013). Observational Evidence of Sausage-Pinch Instability in Solar Corona by Sdo/Aia. *ApJ* 765, L42. doi:10.1088/2041-8205/765/2/l42

Sterling, A. C. (2000). Solar Spicules: A Review of Recent Models and Targets for Future Observations. *SoPh* 196, 79–111. doi:10.1023/a:1005213923962

Tian, H., Deluca, E. E., Cranmer, S. R., De Pontieu, B., Peter, H., Martinez-Sykora, J., et al. (2014). *Sci* 346, 315.

Tsiropoula, G., Tziotziou, K., Kontogiannis, I., Madjarska, M. S., Doyle, J. G., and Suematsu, Y. (2012). Solar Fine-Scale Structures. I. Spicules and Other Small-Scale, Jet-like Events at the Chromospheric Level: Observations and Physical Parameters. *Space Sci. Rev.* 169, 181–244. doi:10.1007/s11214-012-9920-2

Uddin, W., Schmieder, B., Chandra, R., Srivastava, A. K., Kumar, P., and Bisht, S. (2012). Observations of Multiple Surges Associated with Magnetic Activities in Ar 10484 on 2003 October 25. *ApJ* 752, 70. doi:10.1088/0004-637x/752/1/70

Vemareddy, P., and Zhang, J. (2014). Initiation and Eruption Process of Magnetic Flux Rope from Solar Active Region Noaa 11719 to Earth-Directed Cme. *ApJ* 797, 80. doi:10.1088/0004-637x/797/2/80

Weber, M. A., Deluca, E. E., Golub, L., and Sette, A. L. (2004). "Temperature Diagnostics with Multichannel Imaging Telescopes," in *IAU Symp. 223, Multi-Wavelength Investigations of Solar Activity*. Editors A. V. Stepanov, E. E. Benevolenskaya, and A. G. Kosovichev (Cambridge: Cambridge Univ. Press), 2004, 321–328. doi:10.1017/s1743921304006088*Proc. IAU*

Yan, X. L., Yang, L. H., Xue, Z. K., Mei, Z. X., Kong, D. F., Wang, J. C., et al. (2018). *ApJ*, 853, L18.

Yang, K., Guo, Y., and Ding, M. D. (2016). Quantifying the Topology and Evolution of a Magnetic Flux Rope Associated with Multi-Flare Activities. *ApJ* 824, 148. doi:10.3847/0004-637x/824/2/148

Yang, L. P., He, J. S., Peter, H., Tu, C., Zhang, L., Feng, X., et al. (2013). *ApJ*, 777, 16.

Yokoyama, T., and Shibata, K. (1995). Magnetic Reconnection as the Origin of X-ray Jets and Hα Surges on the Sun. *Nature* 375, 42–44. doi:10.1038/375042a0

Zaqarashvili, T. V., and Erdélyi, R. (2009). Oscillations and Waves in Solar Spicules. *Space Sci. Rev.* 149, 355–388. doi:10.1007/s11214-009-9549-y

Zhang, Q. M., and Ji, H. S. (2014). A Swirling Flare-Related EUV Jet. *A&A* 561, A134. doi:10.1051/0004-6361/201322616

Zhang, Q. M., Ji, H. S., and Su, Y. N. (2016). Observations of Multiple Blobs in Homologous Solar Coronal Jets in Closed Loop. *Sol. Phys.* 291, 859–876. doi:10.1007/s11207-016-0878-1

Zhang, Y., and Zhang, J. (2017). Cusp-shaped Structure of a Jet Observed Byirisandsdo. *ApJ* 834, 79. doi:10.3847/1538-4357/834/1/79

Conflict of Interest: The authors declare that the research was conducted in the absence of any commercial or financial relationships that could be construed as a potential conflict of interest.

Publisher's Note: All claims expressed in this article are solely those of the authors and do not necessarily represent those of their affiliated organizations, or those of the publisher, the editors and the reviewers. Any product that may be evaluated in this article, or claim that may be made by its manufacturer, is not guaranteed or endorsed by the publisher.